Initial stage of titanium oxidation in Ti/CuO thermites: a molecular dynamics study using ReaxFF forcefields

Hicham Jabraoui, Alain Estève, Sungwook Hong, Carole Rossi

Initial Stage of Titanium Oxidation in Ti/CuO Thermites: a Molecular Dynamics Study Using ReaxFF Forcefields

Received 00th January 2023,
Accepted 00th January 2023

DOI: 10.1039/x0xx00000x

Hicham Jabraoui[a], Alain Estève[a], Sungwook Hong[b], Carole Rossi[a, †]

The paper elucidates the main driving mechanisms at play during the early stage of the Ti/CuO thermite reaction using reactive forcefields in the frame of molecular dynamics calculations. Results show that TiO preferentially forms in immediate contact to pure Ti at temperatures as low as 200 K rather than TiO_2. Increasing the temperature to 700 K, the 2 nm TiO2 in contact to Ti is found to be homogeneously depleted from half of its oxygen atoms. Also, the first signs of CuO decomposition are observed at 600 K, in correlation with the impoverishment in oxygen atom reaching the titanium oxide layer immediately in contact to CuO. Further quantification of the oxygen and titanium mass transport at temperatures above 700 K suggests that mostly oxygen atoms migrate from and across the titanium oxide interfacial layer to further react with the metallic titanium fuel reservoir. This scenario is opposed to the one of the Al/CuO system, for which the mass transport is dominated by the Al fuel diffusion across alumina. Further comparison of both thermites sheds light into the enhanced reactivity of the Ti-based thermite, for which CuO decomposition is promoted at lower temperature, and offers a novel understanding of thermite initiation at large.

1. Introduction

As a new branch of energetic materials, metal/metal-oxide composites, the so-called thermites, in the form of a powder mixture appeared in the 1990s[1] and gave rise to a large body of work thereafter[2–10]. Unlike CHNO explosives, thermite materials undergo a rapid deflagration driven by a reduction-oxidation type of chemical reaction and possesses a high volumetric energy density (up to 4 kJ. g^{-1}). When ignited, thermite generate an on-demand burst of energy in the form of heat and/or pressure, from which a selection of gaseous species may be utilized. Generally, they are explored to cut[11,12], propel[13,14], disassemble[15,16], weld[17], initiate[18–20], release[21], which actions may be operated under different environments, even in vacuum[22], underwater[23] and in extreme environments[24], for both civilian and military applications. To date, Aluminum (Al) is by far the most common fuel used in thermites because of its high oxidation enthalpy, availability and low cost[25]. Metal oxides, including MoO_3 [26], CuO [27,28], Bi_2O_3 [29], Fe_2O_3[30], I_2O_5[31] have been employed for long as oxidizers, serving as oxygen sources for the metal oxidation. Recently, experimental studies demonstrated superior initiation characteristics of Al-based thermite using titanium fuel additive [32–34] thus bypassing the negative impact of the native alumina (Al_2O_3) coated on aluminum particle limiting mass transport during initiation (i.e., at low temperature, ambient-400°C).[35]

Controlling the initial stage of the thermite chemistry is essential to allow for a number of applications in need of a high responsiveness of the thermite. Shoshin and Dreizin found that the initiation temperature of $Al_{0.75}Ti_{0.25}$ alloys is 969 °C against 1877 °C for neat Al[36]. Zhao and Zachariah found that incorporation of titanium metal into Al/I_2O_5 thermite increases the pressurization rate, i.e., reactivity, by a factor of 1000, and reduces the initiation temperature from ~610 °C to ~300 °C[34]. Very recently, Wu and Rossi experimentally investigated the mechanisms leading to the superior reactivity and ignitability of Ti-based thermites in comparison to Al-based counterpart[37]. They observed a two-step Ti oxidation process occurring starting at low temperature, with an oxidation step of Ti forming TiO, at 300 °C, followed by a second oxidation step turning the TiO layer into TiO_2, at 500 °C. They concluded that these low-temperature exothermal processes are the primary reaction pathways responsible for the low initiation temperature and high reactivity of thermite containing metallic Ti. However, none of these previous experimental results did provide the detailed mechanisms occurring at the interface between CuO and Ti phases, pointing to the formation of unexpected large TiO oxide layers at 300 °C, i.e., well below initiation. The present study uses reactive forcefields (ReaxFF) molecular dynamics (MD) simulations to analyze, at the atomic scale, the structural and chemical transformations accompanying the TiO_x interfacial chemical modification and growth, as this latter plays a critical role in the thermite reactivity, by affecting how species migrate throughout the system before reacting. For that purpose, a $Ti/TiO_2/CuO$ model-system is built to focus on the interface of a compact mixture of Ti and CuO nanoparticles. Simulations are run under various temperature conditions in the 200-900 K range providing detailed atomistic information on the events taking place throughout the material interfaces, as for instance the key migration of both Ti and O species in this system. A key comparison with the Al/CuO thermite is also considered that gives a new perspective towards a universal understanding of thermite initiation.

2. Computational details

All simulations in this paper were performed under the periodic boundary conditions using LAMMPS packages [38]. The temperature and pressure upon MD simulations in the canonical NVT and isothermal-isobaric NPT ensembles are applied using the thermostat and the Nosé-Hoover barostat, respectively. In order to provide interatomic Al-Cu-Ti-O interactions for the entire system within the ReaxFF force field parameters, we combined Al-Cu-O the ReaxFF

[a] LAAS-CNRS, University of Toulouse, 31077 Toulouse, France.
[b] Department of Physics and Engineering, California State University, Bakersfield, Bakersfield, California 93311, United States of America.
† Corresponding Author Carole Rossi E-mail: rossi@laas.fr
Electronic Supplementary Information (ESI) available: [details of any supplementary information available should be included here]. See DOI: 10.1039/x0xx00000x

parameters from Psofogiannakis[39] and Ti-O parametersthose from Kim and van Duin[40]. These merged ReaxFF parameters are given in supporting information S1.

The CuO supercell was built considering a cubic unit cell with lattice parameters a = b = c = 4.23 Å and α = β = γ = 90°[41] which was then replicated in the three spatial directions (x, y, and z) giving a CuO slab containing 640 O atoms and 640 Cu atoms. This constructed CuO supercell was subjected to a first thermal relaxation at 300 K in the NPT ensemble over 0.1 ns reaching an XY area of 23.46 Å × 23.46 Å, followed by a second relaxation at 300 K in the NVT ensemble over 0.1 ns. This length of time was found to be sufficient to ensure the equilibration of both the total energy and cell volume. The relaxed CuO structure was cleaved perpendicular to the [001] direction giving rise to polar Cu rich and oxygen rich CuO (001) surfaces. In this study, the Cu-rich surface is considered as the bottom surface slab with atomic positions frozen in their lattice sites to mimic a bulk material constraint. The top slab layer is therefore oxygen rich, as the model surface mostly used and documented in the literature, experimentally[42], and theoretically[43,44]. The choice of the CuO(001) surface was strongly recommended by the recent DFT investigation by Jabraoui et al.[43], showing that the CuO(001) offers unique capability to release oxygen species issued from bulk CuO, which process requires oxygen vacancies to promote oxygen transport at an acceptable temperature (< 600 K, atmospheric pressure), in agreement with experimental findings. In this context, we created a defective CuO surface by distributing 2.4% of oxygen vacancies (removal of 16 oxygens) at the vicinity of the surface, in accordance with ref. [43]. To obtain stable configurations despite the presence of oxygen vacancies, this defective CuO was subjected to a minimization step using the conjugate gradient (CG) algorithm[45] and then relaxed again at 300 K in the NVT ensemble over 0.1 ns. It has to be noted that a validation step of the CuO forcefield was operated making systematic comparison with published DFT results on bulk, subsurface and CuO (001) surface (**Figure S1**) in a manner to evaluate its capability to treat decomposition processes. For providing realistic simulations, a pristine amorphous metallic oxide (*am*TiO_2) was added on top of the metallic Ti slab [46]. *am*TiO_2 was built by performing non-reactive MD simulations based on the Morse formulation [47] coupled with long-range Coulomb interactions. The last term was computed using the Ewald summation with a cutoff of 12.0 Å for the real part with a desired relative error in forces less than 10^{-6}, while the short-range cutoff was set to 8.0 Å[48–52]. The initial atomic structures were constructed by randomly distributing 700 atoms (300 Al and 450 O for *am*Al_2O_3, and 250 Ti and 500 O for *am*TiO_2) in simulation boxes. These boxes were fitted to the XY dimensions of the CuO slab. These initial atomistic models were first relaxed at 3500 K in the NPT ensemble over 1 ns while only the Z direction of the simulation box was left in equilibrium, in order to obtain the correct volume. The simulation box with a new dimension in the Z direction underwent another relaxation at the same temperature for 0.1 ns in the NVT ensemble to obtain our full equilibrium liquid state, which was then submitted to a quenching step with a rapid cooling rate of 10 K .ps^{-1} in the NPT ensemble to reach the glassy state at 300 K[49,52,53]. Finally, the glassy state was relaxed at 300 K over 0.1 ns. The *am*TiO_2 surface was then cleaved in the Z direction and further annealed at 300 K for 1 ns in the NVT ensemble, before being added to the Ti metal cell to form the desired Ti-*am*TiO_2 stacking. Ti metallic region contains 2016 atoms in a face-centered cubic crystal structure [54,55]. A final chemical stabilization of the interface between Ti and *am*TiO_2 was realized through annealing in the NVT ensemble at 200 K over 1 ns.

Finally, the CuO surface is concatenated with the Ti-*am*TiO_2 to form the overall thermite system: Ti/*am*TiO_2/CuO. A void in the Z direction of 26 Å was added over the metallic region to avoid any interaction between Ti and CuO layers (**Figure 1**). Both of these models underwent a final relaxation step at 200 K in the NVT ensemble for 1 ns to chemically stabilize all surfaces where the bottom layers of the entire supercell are on the CuO side kept frozen throughout the simulation. The time step is 1 fs for any simulation run in this study.

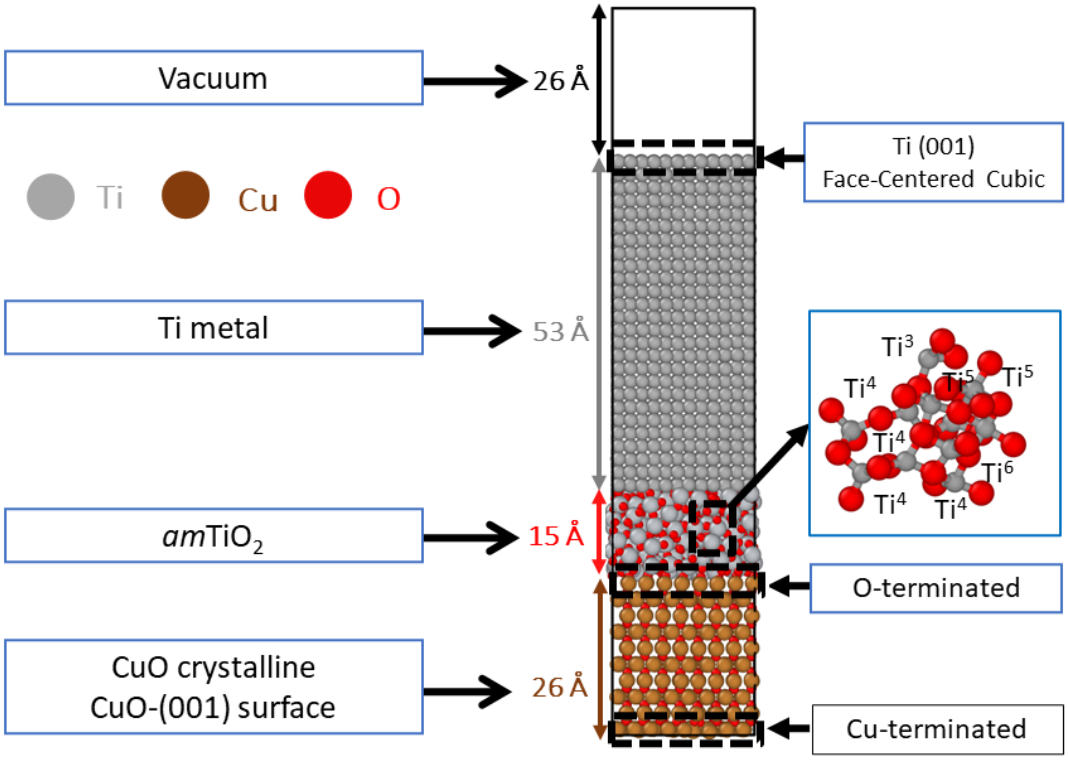

Figure 1. Schematic of the side-view of the initial (pre-annealed) atomic scale model of the Ti/CuO nanothermite, also referred as Ti/*am*TiO_2/CuO, as an initial *am*TiO_2 layer separates CuO from Ti.

3. Results and discussions

The Ti/*am*TiO_2/CuO structure was heated from 200 K to selected temperatures, ranging from 400 to 900 K at a heating rate of 10^{13} $K.s^{-1}$, followed by 5 ns annealing duration. This length of time was found sufficient to reach a steady state (generally obtained after ~3 ns, see **Figure S2**).

3.1. Formation of the TiO interface between the layers of Ti and TiO2

Figure 2 shows side view snapshots of the post-annealed Ti/*am*TiO_2/CuO structure at the temperatures of 500 K (b), 700 K (c) and 900 K (d), in comparison with the structure at 200 K (a). Upon annealing, the initial *am*TiO_2 layer separating CuO from Ti changes in thickness and stoichiometry, thus labelled TiO_x (with $1< x < 2$) in the rest of the paper.

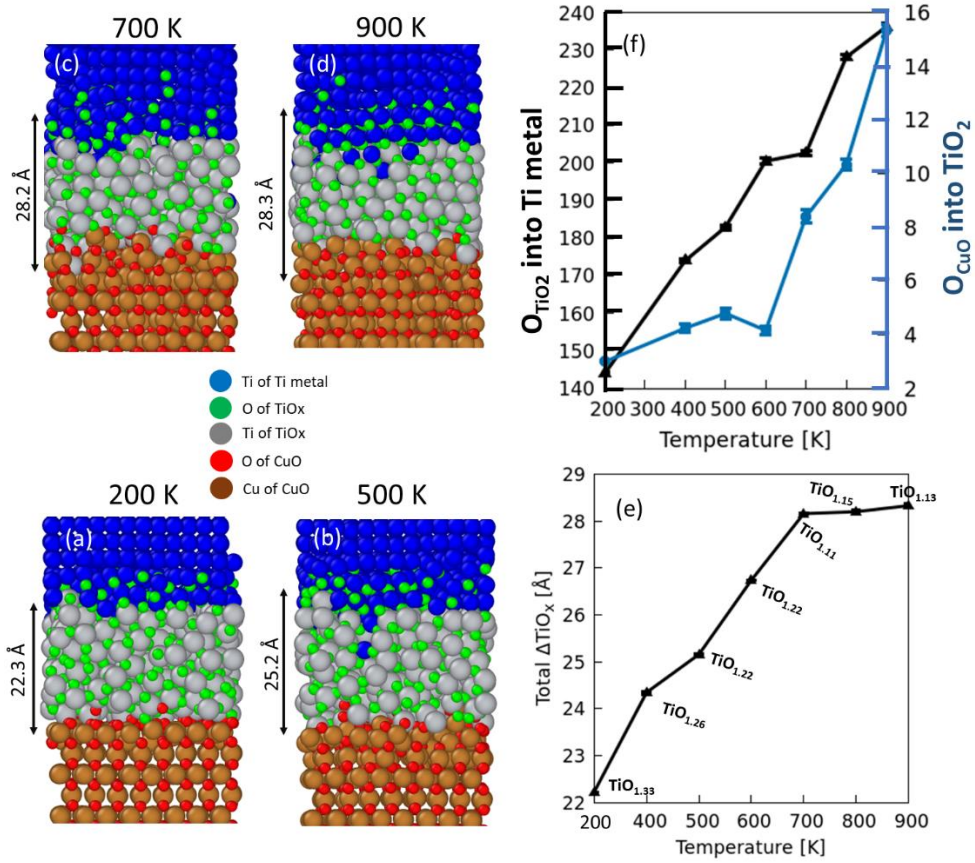

Figure 2. (a-d) Side view snapshots of the initial (pre-annealed) and final (post-annealed) structures at different temperatures (200, 500, 700, and 900 K), respectively. (e) The total TiO_x thickness as a function of temperature. (f) The average number of oxygens originally belonging to pristine *am*TiO_2 (red balls, Ti from the oxide) that have migrated into the Ti metal (blue balls) and the averaged amount of O originally belonging to CuO (green balls) that have migrated into the new TiO_x region, at different temperatures. Average values were computed over the last 100 ps of the annealing stages.

The first observation is the continuous expansion of the titanium oxide region due to the spontaneous reaction of oxygen atoms from titania with the metallic titanium atoms belonging to the Ti fuel reservoir. Results show that this process starts at very low temperature. At 200 K the *am*TiO_2 has released a reasonable number of its oxygen atoms which further penetrate and oxidize approximately two layers of the pure titanium reservoir. In doing so, we can assume that Ti cannot share an abrupt epitaxial interface with TiO_2 at room temperature. In the 200-600 K temperature range, the Ti/TiO_x structure continuously modifies: ~140-170 oxygens (out of 450 oxygen originally belonging to *am*TiO_2) migrate from *am*TiO_2 into the pure Ti layers (**Figure 2f**). This is to be compared with CuO, which loses only 4 oxygen atoms migrating into the *am*TiO_2 within this temperature range. At 700 K, 40% (~200 atoms) of the oxygen atoms originally belonging to *am*TiO_2 migrate into metallic Ti so that the initial *am*TiO_2 region turns into a $TiO_{1.1}$, *i.e.*, close to the TiO stoichiometry (**Figure 2e**), accompanied with a thickening of the oxide interfacial region. The interface reaches 28 Å thick, which represents almost 30 % of thickness inflation. Interestingly, the depletion of the initial *am*TiO_2 layer stops when the titanium monoxide (TiO) stoichiometry is reached indicating that TiO constitutes a chemically stable oxide interface in contact to Ti, as observed from low temperatures. The Ti-O interatomic distance and average coordination number (ACN) are 1.88-2.10 Å and ~4, respectively, close to the typical Ti-O bond distance in the titanium monoxide glassy state rather than in the titanium dioxide glassy state, in accordance with previous spectroscopy-DFT combination studies [56,57] (**Figure S3)**. A closer look at the structure of TiO_x after annealing at the different temperatures (Ti atoms are colored by coordination numbers, **Figure 3g**) compared with the model glassy oxides of TiO and TiO_2 (**Figure 3f**) confirm the chemical evolution of the oxide interfacial layer, from a TiO_2 to a TiO. In addition, the low coordination numbers of Ti bring another confirmation of the TiO_2 to TiO transition. It has to be noted that Ti^2 is absent at 400 K and below, which is expected as this species is not present in glassy TiO_2 and appears when stoichiometry approaches the TiO one. Same effect goes with Ti^3, but a rough equilibration is reached starting from 400 K. For the Ti^6 high coordination, it is lost below the ambient temperature proving that the reduction of the *am*TiO_2 is well operated starting at low temperature. The quantity of Ti^5 increases

with increasing temperature; a total of 58% of increase is calculated, which is to be compared with the 56% increase values calculated comparing ideal glassy TiO and TiO_2 model systems. Finally, the vanishing of Ti^6 is another confirmation of the TiO_2 → TiO transition upon annealing at 700 K, as Ti^6 is absent from glassy TiO model system shown in **Figure 3f**. From **Figure 3g**, even though the TiO_x layer homogenizes, decreasing overall coordination as the temperature increases, still the interface with CuO shows higher coordination, which is further detailed in the next section.

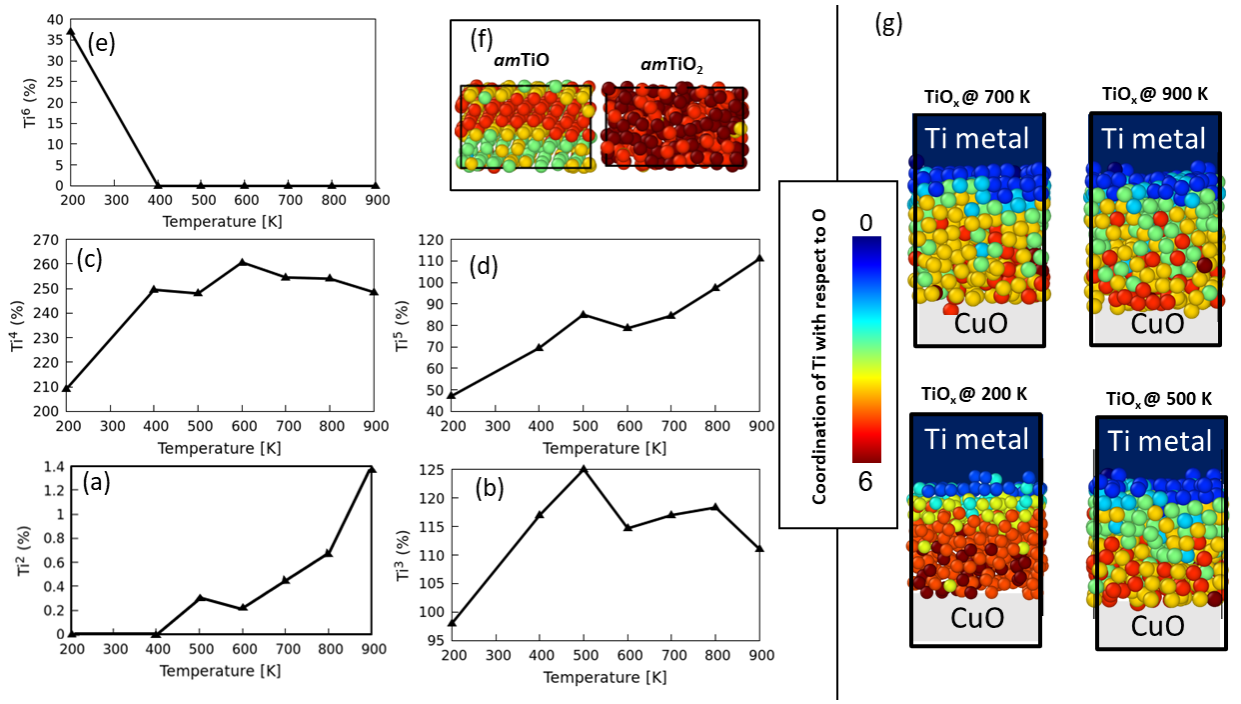

Figure 3. (a-e) Amount of Ti^2, Ti^3, Ti^4, Ti^5 and Ti^6 ions relative to the coordination number to neighboring O atoms in the evoluting TiO_x region, as a function of temperature, respectively. Values were averaged over the last 0.5 ns of annealing. (f) Snapshots of both glassy TiO_2 and TiO glassy state model systems for comparison. (g) Snapshots of the Ti/TiO_x/CuO after the annealing process over 5 ns at 200 K, 500 K, 700 K and 900 K, showing the distribution of different types of Ti ions coordination (Ti^n) in the TiO_x region. Note that CuO is shaded for clarity of presentation.

3.2. CuO decomposition starting at 600 K

The chemical evolution of the TiO_2/Ti interface, from 200 K to 700 K, differs from that of CuO/TiO_2. In this latter interface, at 200 K, only anecdotic atomic rearrangements occur mainly inferred to local rather than global interface chemical stabilization; only ~ 4 O-Cu bonds break and both O and Cu atoms rearrange chemically at the CuO/TiO_2 interface, which remains then stable until 600 K (**Figure 2f**). At 800 K, the number of oxygen atoms released from CuO, increases to 8 which corresponds to only 8% of a single oxygen monolayer of the CuO crystal. To shed light into the CuO modification at the vicinity of the interface, we consider only a 7 Å thick CuO/TiO_x slab. This enables to avoid screening of the interfacial trends by the larger bulk CuO region that do not show significant chemical and structural modification. As the coordination does not allow distinguishing between CuO and Cu_2O phases, the interatomic distances and pair correlation functions for both Cu-O and Cu-Cu interatomic distances are analyzed in **Figure 4**. It is interesting to note that the Cu-O bond starts decreasing quasi linearly from 1.86 Å at 500 K characteristic of CuO, to 1.81 Å at 900 K. This Cu-O interatomic distance reduction is consistent with the reduction of the copper oxide layer at the interface. Similarly, for Cu-Cu interatomic distance characteristic of bulk CuO at 200 K, a redistribution of copper atoms of the top CuO layer is taking place resulting in a significant reduction of the distance from ~3 to 2.6 Å. This process is relatively similar to the reconstruction of the CuO(001) free surface observed using DFT calculations, for which the well aligned Cu top surface layer splits in the direction perpendicular to the surface [43]. Careful visualization of the CuO/TiO_x interface structure allows following this splitting process, which is partial at 500 K (**Figure 2b**), and continuously progresses to end up with the splitting of the full Cu monolayer into two Cu layers at 900 K (**Figure 2d**). The step increase can be seen as an indication of CuO reduction going on as the temperature increases, following a trend similar to the Cu-O interatomic distance evolution towards reduction.

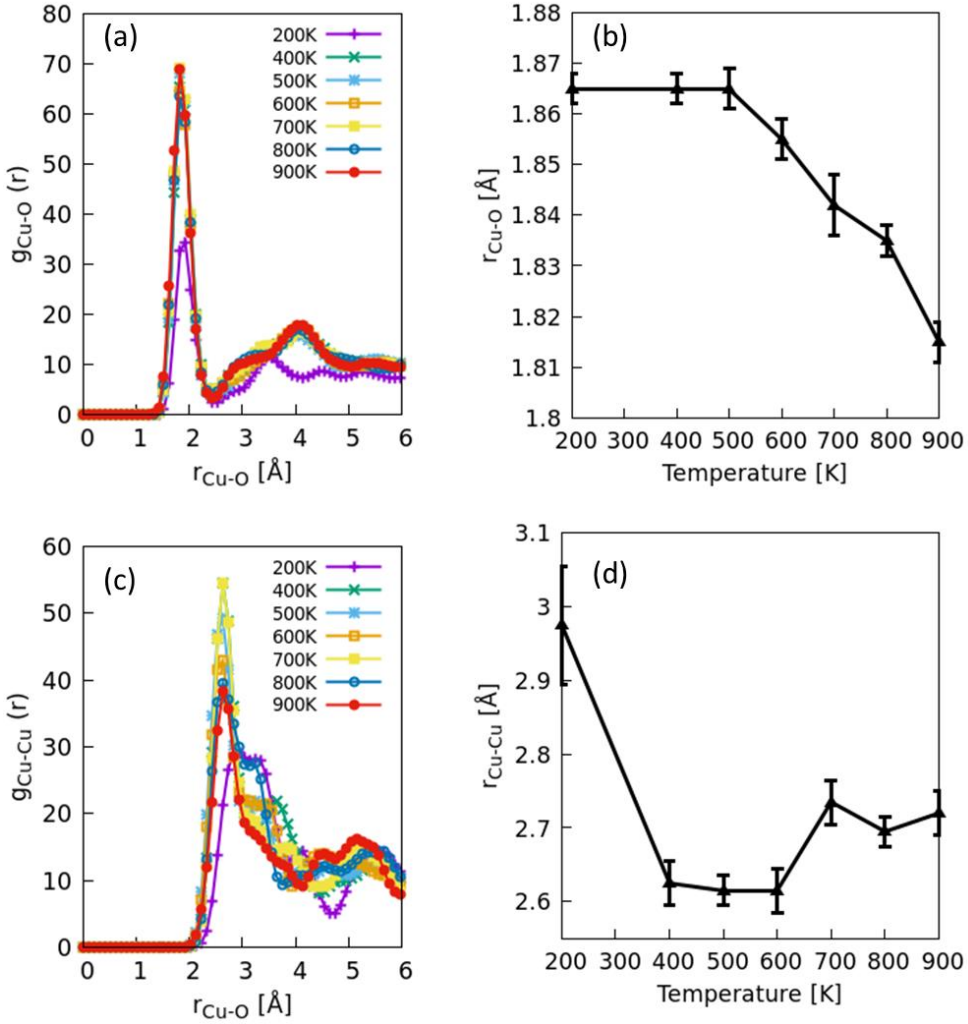

Figure 4. Cu-O (a-b) and Cu-Cu (c-d) radial distribution functions (RDF) and interatomic distances, all located at the CuO-TiO_x interface. RDFs and bond lengths were obtained from averaging over the last 0.5 ns of annealing stages.

Importantly, the Cu-Cu interatomic distance reaches ~2.7 Å at the temperature when TiO is formed, i.e., at 700 K (**Figures 2** and **4**). This might indicate that the richness of the titanium oxide in oxygen is one major actor of CuO reduction. Further annealing at 900 K shows greater migration of oxygen atoms from copper oxide to titanium oxide region (**Figure 2f**). The system evolution at high temperature and over time is studied in the following section.

3.3. Interface evolution at higher temperatures extrapolated from diffusion investigation

The decomposition of CuO, which is a prerequisite to initiating the thermite reaction is not clearly established in our simulations, because the decomposition process is kinetically slow and unreachable within 5 ns. To overcome this issue and extrapolate a tendency, the diffusion of species across the different interfacial layers that show intermixing is estimated in the temperature range of 400-900 K. First, we computed the diffusion coefficients of oxygen originally belonging to CuO (OBC) and the Ti originally belonging to the metallic titanium (TBM) contributing to the growth of TiO_x. Then, in order to quantify atomic diffusion, mean square displacement (MSD) was estimated, using the following equation[58–60]:

$$\mathrm{MSD} = < \delta r^2 > \; = \frac{1}{N}\sum_i [r_i(t + t_0) - r_i(t_0)]^2 \qquad (1)$$

Where N is the total number of atoms to be studied statistically, the two parameters $r_i(t_0)$ and $r_i(t + t_0)$ are the displacements of atom i at time (t_0) and time $(t + t_0)$, respectively. After calculating the MSD for a set of targeted atoms, Einstein's relation fitted to three-dimensional material was used to determine the self-diffusion coefficient (D) as follows[58,59].

$$D = \lim_{t \to 0} \frac{<\delta r^2>}{6t} = \lim_{t \to 0} \frac{<\mathrm{MSD}>}{6t} \qquad (2)$$

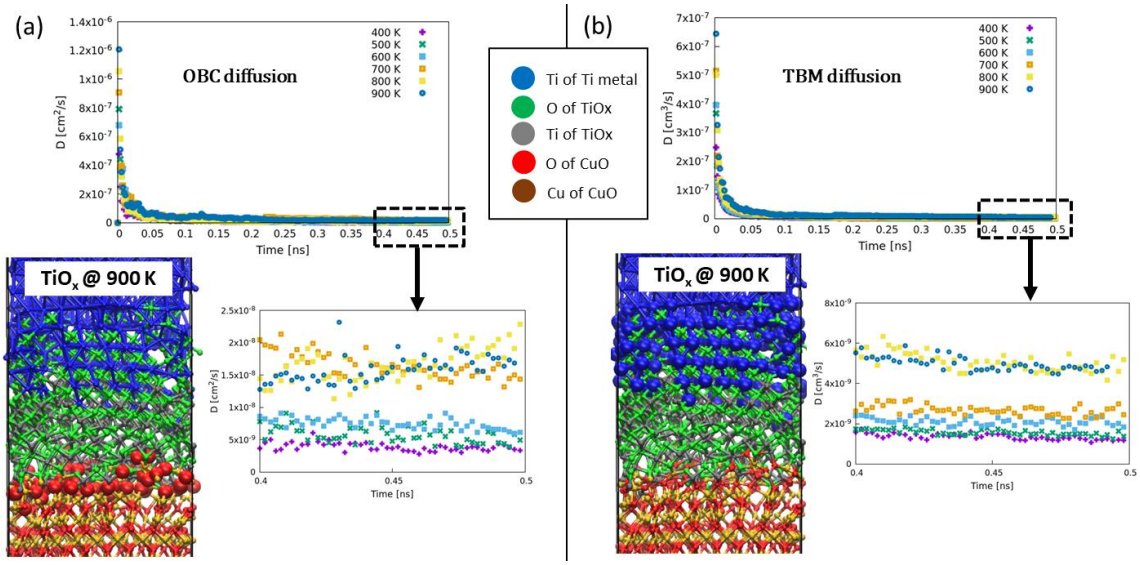

Figure 5. (a-b) Diffusion coefficients of oxygen (large red balls) in left snapshot, and titanium (large blue balls) in right snapshot, initially belonging respectively to Cu (OBC), and metallic fuel (TBM) in the TiO_x interface, at different temperatures (400-900 K).

Figure 5, plots the diffusion of the main migrating atomic species, namely OBCs and TBMs, with the final structure captured at the last simulation snapshot of the 900 K annealing. The diffusion of these atoms was computed and averaged over the last 0.5 ns of the annealing process for which the equilibrium is reached. The diffusion coefficients were computed after annealing in the range 400-900 K, as reported in **Figure 5**. Results show an asymmetric behavior of both interfaces. The diffusion of OBC atoms in the TiO_x region is activated at 700 K with a diffusion being 3 times higher than that at low temperature (≤ 700 K), as seen in **Figure 5a** and **Table 1**. Noteworthy, this activation in TiO_x correlates well with the modification of interfacial CuO that start deoxidizing in a more significant manner, and the stabilization of the Cu-Cu first neighbor bond length at 2.7 Å. TBM atoms diffusion is activated at 800 K, with a diffusion coefficient 3 times below than that of OBC. It has to be noted that the diffusion of oxygen atoms from CuO is higher than that of Ti at all annealing temperatures, particularly after activation (**Table 1**). Reaching 900 K, we also calculated the diffusion coefficient of titanium being close to the CuO layers. With a value of 8.9×10^{-9} cm²/s, compared to 4.98×10^{-9} cm²/s for the less mobile TBMs, the CuO/TiO_x interface appears much more chemically active than the Ti/TiO_x interface. This might prefigure the decomposition of CuO and massive insertion of oxygen, turning the interfacial TiO_x in contact to CuO to a higher coordination, as clearly visible from the atomistic snapshot in **Figure 2g** and counting of Ti^5 in **Figure 3d**. This trend towards CuO decomposition finds confirmation in the comparison of OBC oxygen diffusion, equal to 16.0×10^{-9} cm²/s, with slower oxygen atoms taken at the vicinity of the CuO interface (TiO_x deepest layers), calculated to be 8.9×10^{-9} cm²/s.

Table 1 Diffusion coefficients of the titanium originally belonging to metallic fuel (TBM) and of the oxygen originally belonging to CuO (OBC) participating to the growth of the TiO_x region

T (K)	OBC atoms		TBM atoms	
	D (cm²/s) ×10⁻⁹	δD (cm²/s) ×10⁻⁹	D (cm²/s) ×10⁻⁹	δD (cm²/s) ×10⁻⁹
400	3.88	1.35	1.35	$8.9\ 10^{-2}$
500	5.75	2.11	2.11	$1.8\ 10^{-1}$
600	7.50	1.57	1.57	$1.2\ 10^{-1}$
700	16.4	2.69	2.69	$2.7\ 10^{-1}$

800	23.4	5.07	5.07	$2.7\ 10^{-1}$
900	16.0	4.98	4.98	$2.9\ 10^{-1}$

3.4. Ti/*am*TiO_2/CuO versus Al/*am*Al_2O_3/CuO system

Main findings of section 3.1. are that (i) TiO_2 cannot form an abrupt and stable interface with pure titanium, even at the ambient; (ii) oxygen is the migrating species instead of metallic Ti. Results also highlighted that the titanium oxide layer in contact with the CuO remains stable up to 600 K, i.e., it remains in the form of a *am*TiO_2 glassy state (**Figure 3g**), which corroborates recent experimental findings by T. Wu *et al.* [37] on the structural and chemical characterization of the growing interface in Ti/CuO nanolaminate. The authors showed that Ti is oxidized in TiO at 600 K, and further oxidized into crystalline TiO_2 after annealing at 800 K. In addition, the authors did not observe migration of Ti and concluded that oxygens are the sole migrating species below 800 K in Ti/CuO nanolaminates. In this last section, we find interesting to compare the above described Ti/CuO mechanistic pre-initiation scenario with the very well documented Al/CuO fully-dense material [61-64]. It is now well documented that in this latter reactive system, reactions leading to the initiation results from the diffusion of Al ions and counter-diffusion of oxygens released by the CuO decomposition. This process was shown to transform the stoichiometric alumina into a more chemically active Al rich alumina, inducing counter migration of oxygen atoms from the copper oxide[63]. By contrast, in Ti/CuO system, the growing TiO interfacial layer, becomes an oxygen sink for oxygen atoms from CuO, which could favor the CuO decomposition. This conjecture can be characterized by comparing the diffusion parameters of Ti, O and Al at specific locations, in the interfaces, between Al/CuO and Ti/CuO systems, at 600 and 700 K (**Figure 6**). Ti shows the slowest diffusion coefficient compared to O and Al, with 2.7×10^{-9} $cm^2.s^{-1}$ at 700 K (Ti/CuO system). Diffusion coefficient of oxygen reaches 7.5 and 16.4 $\times 10^{-9}$ $cm^2.s^{-1}$ at 600 and 700 K, respectively. It has to be noted that the diffusion of O increases with the temperature by a factor of 6. At 700 K, Ti penetrates into the CuO region, but in insignificant amount (**Figure 6d**).

In the Al/CuO system, we found that the penetration of Al atoms into the interfacial layer reaches its maximum level at ~900 K. Indeed, Al reached the CuO surface which activates the CuO reduction and growth of the Al_xO_y interface into the CuO (**Table S1, Figure S4**). Finally, **Figure 6** shows that the TiO_x growth is more pronounced than that of Al_xO_y, correlated with the greater mixing at the Ti/TiO_x interfaces than that of the Al/Al_xO_y interfaces, caused by a higher oxygen to titanium affinity compared to that of titanium with aluminum[63].

A static study by DFT calculations reported that the first-second interlayer contractions adjacent to the CuO substrate are approximately 2.1% for the layers of aluminum and 8.6% for titanium layers[56]. While both systems show differences in the migrating actors, one fundamental aspect that is common to both systems is that CuO decomposition, or initiation, activates through chemical modification of their interfacial layer separating the fuel from the oxidizer: titanium oxide is reduced to TiO and aluminum oxide is enriched in Al. These processes are presumably the first step that chemically activate the decomposition of CuO. In this view point, decomposition of CuO differs in both systems, as for the reducing agent in immediate contact to CuO, either Al rich Al_2O_3 or titanium monoxide.

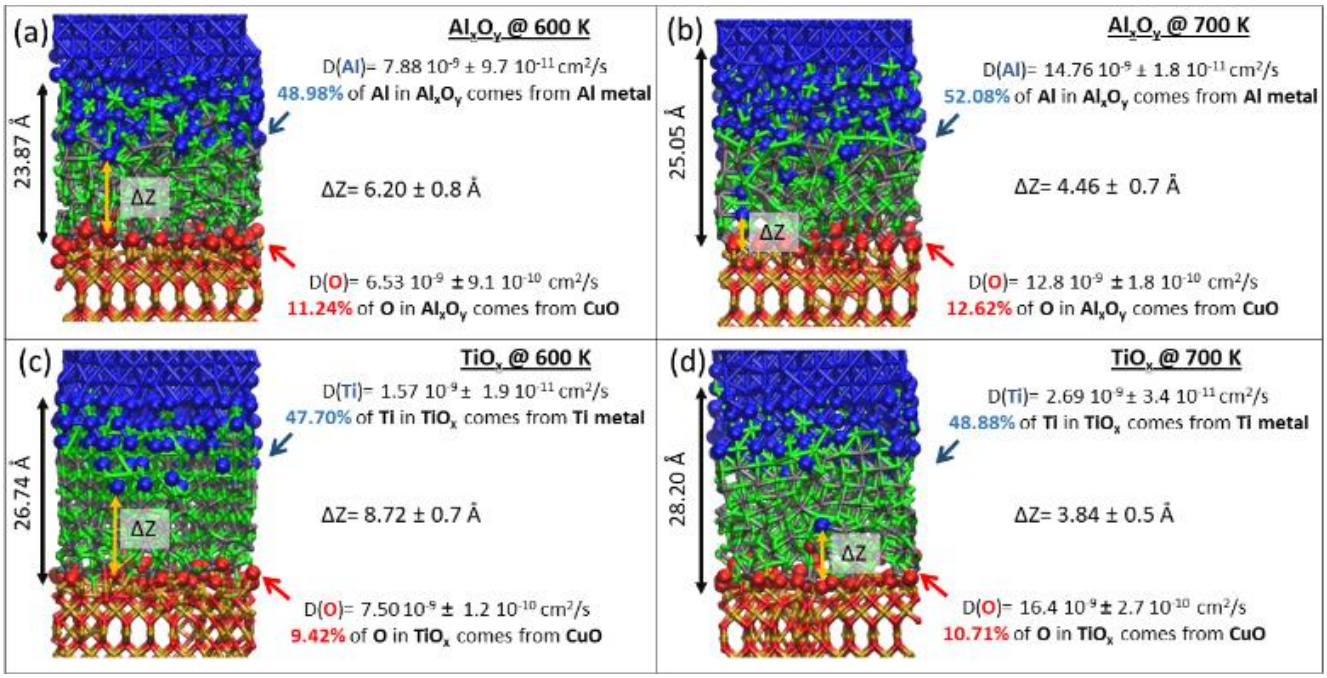

Figure 6. Side view snapshots of the final (post-annealed) structures at 600 K and 700 K for Al_xO_y (top) and TiO_x (bottom) interfacial regions. These two temperatures represent the growth activation temperature range for the metal oxide mixture in Ti/CuO nanothermite and Al/CuO, respectively. For each temperature and structure, are indicated, the percentage of oxygen originally belonging to CuO (red) and the percentage of Ti or Al originally .

belonging to the metallic fuel at the oxide interface (blue), as well as their diffusion coefficient (D), and, the level of penetration of the metallic fuel Ti or Al (ΔZ) in the oxide interface, and, the percentage of oxygen and Ti/Al atoms integrated in the newly created metal oxide region as obtained by averaging values estimated from the last 0.5 ns of annealing steps.

4. Conclusions

This paper presents a ReaxFF Molecular Dynamics study that describes the structural and chemical transformations occurring at the Ti/CuO interfaces upon heating up to 900 K. For that purpose, a 5.3 nm × 1.5 nm × 2.5 nm Ti/*am*TiO_2/CuO was built and utilized as a model-system representing the interface of a compact mixture of Ti and CuO particles. The main findings are: i) at low temperature (200 K) the initial *am*TiO_2 layer in contact to pure Ti is spontaneously reduced and gradually replaced by a thicker TiO_x ($x < 2$) upon increasing the temperature. TiO_x grows and expand across the metallic Ti region, ii) at high temperature (≥ 700K), the rate of oxygen atoms engaged in diffusion towards Ti is multiplied by a factor of 3 compared with temperature ≤ 400 K. This leads to the formation of a TiO phase in place of the initial *am*TiO_2 layer. The reduced titanium oxide layer activates oxygen uptake from CuO that starts decomposing. Results also showed that, upon heating, Ti/*am*TiO_2/CuO system behaves differently from Al/*am*Al_2O_3/CuO, which explains the experimental difference observed on Ti/CuO and Al/CuO nanothermites. At the early stage of initiation, while oxygen atoms migrate towards the titanium reservoir in the case of Ti/*am*TiO_2/CuO, Al atoms migrate from the Al reservoir in Al/*am*Al_2O_3/CuO. In both cases, these atomic migrations modify the thickness and chemical nature of the interfacial layer acting as barrier layer between the metal and the CuO, namely AlO_x and TiO_x. Importantly, in both cases, the AlO_x and TiO_x evolve toward metallic rich oxides, which in turn favors oxygen uptake from CuO. Examination of diffusion parameters through these interfaces is correlated to the higher reactivity of Ti-based thermites, as observed experimentally.

Electronic Supplementary Information

(i)Comparison of the ReaxFF and DFT approaches in terms of oxygen diffusion in CuO calculated by NEB (Nudged Elastic Band) approximations in order to show the reliability of ReaxFF parameters for reproducing CuO oxygen reduction processes in MD simulations as a major step in ignition of Ti/CuO or Al/CuO nanothermite, (ii) thermalization simulations and more details on the characterization of Ti/CuO and Al/CuO nanothermites, and (iii) parameters ReaxFF used to simulate Ti/CuO and Al/CuO nanothermites.

Author Contributions

All authors contributed equally in this work.

Conflicts of interest

The authors declare no competing financial interests.

Funding sources

C.R. received funding from the European Research Council (ERC) under the European Union's Horizon 2020 research and innovation program (grand agreement No. 832889 - Pyrosafe).

Acknowledgements

The authors grateful acknowledge support from the European Research Council (H2020 Excellent Science) Researcher Award (grant 832889 – PyroSafe). This work was performed using high power computing resources from CALMIP.

References

1 L. L. Wang, Z. A. Munir and Y. M. Maximov, *Journal of Materials Science*, 1993, **28**, 3693–3708.
2 M. L. Pantoya and J. J. Granier, *Propellants, Explosives, Pyrotechnics*, 2005, **30**, 53–62.
3 L. Wang, D. Luss and K. S. Martirosyan, *Journal of Applied Physics*, 2011, **110**, 074311.
4 M. Polis, A. Stolarczyk, K. Glosz and T. Jarosz, *Materials*, 2022, **15**, 3215.
5 X. Zhou, M. Torabi, J. Lu, R. Shen and K. Zhang, *ACS Appl. Mater. Interfaces*, 2014, **6**, 3058–3074.
6 J. Zapata, A. Nicollet, B. Julien, G. Lahiner, A. Esteve and C. Rossi, *Combustion and Flame*, 2019, **205**, 389–396.
7 E. L. Dreizin, *Progress in Energy and Combustion Science*, 2009, **35**, 141–167.
8 M. J. Abere, M. T. Beason, R. V. Reeves, M. A. Rodriguez, P. G. Kotula, C. E. Sobczak, S. F. Son, C. D. Yarrington and D. P. Adams, *Journal of Applied Physics*, 2022, **132**, 035305.
9 V. E. Sanders, B. W. Asay, T. J. Foley, B. C. Tappan, A. N. Pacheco and S. F. Son, *Journal of Propulsion and Power*, 2007, **23**, 707–714.
10 Y. Jiang, H. Wang, J. Baek, D. Ka, A. H. Huynh, Y. Wang, M. R. Zachariah and X. Zheng, *ACS Nano*, 2022, **16**, 14658–14665.
11 L. Glavier, A. Nicollet, F. Jouot, B. Martin, J. Barberon, L. Renaud and C. Rossi, *Propellants, Explosives, Pyrotechnics*, 2017, **42**, 308–317.
12 A. Nicollet, L. Salvagnac, V. Baijot, A. Estève and C. Rossi, *Sensors and Actuators A: Physical*, 2018, **273**, 249–255.
13 C. S. Staley, K. E. Raymond, R. Thiruvengadathan, S. J. Apperson, K. Gangopadhyay, S. M. Swaszek, R. J. Taylor and S. Gangopadhyay, *Journal of Propulsion and Power*, 2013, **29**, 1400–1409.
14 R. Ramachandran, V. S. Vuppuluri, T. J. Fleck, J. F. Rhoads, I. E. Gunduz and S. F. Son, *Propellants, Explosives, Pyrotechnics*, 2018, **43**, 258–266.
15 F. Sevely, T. Wu, F. S. Ferreira de Sousa, L. Seguier, V. Brossa, S. Charlot, A. Esteve and C. Rossi, *Sensors and Actuators A: Physical*, 2022, **346**, 113838.
16 S. K. Pandey and S. Mukherjee, in *2013 IEEE 5th International Nanoelectronics Conference (INEC)*, 2013, pp. 353–356.
17 D. M. B. Dombroski, A. Wang, J. Z. Wen and M. Alfano, *Journal of Manufacturing Processes*, 2022, **75**, 280–300.
18 L. Salvagnac, S. Assie-Souleille and C. Rossi, *Nanomaterials*, 2020, **10**, 2009.
19 P. Zhu, G. Hou, H. Wang, C. Xu, S. Zhao and R. Shen, *Journal of Microelectromechanical Systems*, 2018, **27**, 1186–1192.
20 J. Xu, Y. Tai, Y. Shen, J. Dai, W. Xu, Y. Ye, R. Shen and Y. Hu, *Sensors and Actuators A: Physical*, 2019, **296**, 241–248.
21 C. Rossi, *Propellants, Explosives, Pyrotechnics*, 2019, **44**, 94–108.
22 Thermite-for-Demise (T4D): Concept Definition for Exothermic Reaction-Aided Spacecraft Demise During Re-Entry, https://re.public.polimi.it/handle/11311/1221288, (accessed October 7, 2022).
23 H. L. Li, D. Liu, N. Guo, H. Chen, Y. P. Du and J. C. Feng, *Journal of Materials Processing Technology*, 2017, **245**, 149–156.
24 O. Odawara, T. Fujita, A. V. Gubarevich and H. Wada, *Int. J Self-Propag. High-Temp. Synth.*, 2018, **27**, 228–235.
25 J. Weritz and M. Dudek, in *REWAS 2022: Developing Tomorrow's Technical Cycles (Volume I)*, eds. A. Lazou, K. Daehn, C. Fleuriault, M. Gökelma, E. Olivetti and C. Meskers, Springer International Publishing, Cham, 2022, pp. 3–6.
26 J. J. Granier and M. L. Pantoya, *MRS Online Proceedings Library*, 2003, **800**, 185–190.
27 H. Wang, G. Jian, G. C. Egan and M. R. Zachariah, *Combustion and Flame*, 2014, **161**, 2203–2208.
28 S. M. Umbrajkar, M. Schoenitz and E. L. Dreizin, *Thermochimica Acta*, 2006, **451**, 34–43.
29 W. Yajun, J. Zisheng and F. Changgen, *Progress in Chemistry*, 2016, **28**, 391.
30 J. L. Cheng, H. H. Hng, H. Y. Ng, P. C. Soon and Y. W. Lee, *Journal of Physics and Chemistry of Solids*, 2010, **71**, 90–94.
31 A. Prakash, A. V. McCormick and M. R. Zachariah, *Nano Lett.*, 2005, **5**, 1357–1360.
32 X. Zhu, M. Schoenitz and E. L. Dreizin, *Oxid Met*, 2006, **65**, 357–376.
33 W. Zhao, H. Wang, D. J. Kline, X. Wang, T. Wu, J. Xu, H. Ren and M. R. Zachariah, *Chemical Engineering Journal*, 2022, **438**, 134837.
34 W. Zhao, X. Wang, H. Wang, T. Wu, D. J. Kline, M. Rehwoldt, H. Ren and M. R. Zachariah, *Combustion and Flame*, 2020, **212**, 245–251.
35 T. Wu, G. Lahiner, C. Tenailleau, B. Reig, T. Hungria, A. Esteve and C. Rossi, *Chemical Engineering Journal*, 2021, **418**, 129432.
36 Y. L. Shoshin and E. L. Dreizin, *Combustion and Flame*, 2006, **145**, 714–722.
37 T. Wu, V. Singh, B. Julien, C. Tenailleau, A. Estève and C. Rossi, *Chemical Engineering Journal*, 2022, **453**, 139922.
38 S. Plimpton, *Journal of Computational Physics*, 1995, **117**, 1–19.
39 G. M. Psofogiannakis, J. F. McCleerey, E. Jaramillo and A. C. T. van Duin, *J. Phys. Chem. C*, 2015, **119**, 6678–6686.
40 S.-Y. Kim and A. C. T. van Duin, *J. Phys. Chem. A*, 2013, **117**, 5655–5663.
41 H. Cao, Z. Zhou, J. Yu and X. Zhou, *J Comput Electron*, 2018, **17**, 21–28.
42 L. Liang, K.-Y. Niu, L. Zhang, J. Tian, K. Zhou, X.-L. Wang, X.-M. Zhang and M. Hong, *ACS Appl. Nano Mater.*, 2021, **4**, 6135–6144.
43 H. Jabraoui, M. Djafari Rouhani, C. Rossi and A. Esteve, *Phys. Rev. Materials*, 2022, **6**, 096001.
44 C. Zheng and H. Zhao, *Proceedings of the Combustion Institute*, 2021, **38**, 5281–5288.
45 E. Bitzek, P. Koskinen, F. Gähler, M. Moseler and P. Gumbsch, *Phys. Rev. Lett.*, 2006, **97**, 170201.
46 K. Shimizu, R. C. Furneaux, G. E. Thompson, G. C. Wood, A. Gotoh and K. Kobayashi, *Oxid Met*, 1991, **35**, 427–439.
47 A. Pedone, G. Malavasi, M. C. Menziani, A. N. Cormack and U. Segre, *J. Phys. Chem. B*, 2006, **110**, 11780–11795.

48 H. Jabraoui, T. Charpentier, S. Gin, J.-M. Delaye and R. Pollet, *J. Phys. Chem. C*, 2021, **125**, 7919–7931.
49 H. Jabraoui, M. Malki, A. Hasnaoui, M. Badawi, S. Ouaskit, S. Lebègue and Y. Vaills, *Phys. Chem. Chem. Phys.*, 2017, **19**, 19083–19093.
50 E. M. Ghardi, H. Jabraoui, M. Badawi, A. Hasnaoui, S. Ouaskit and Y. Vaills, *J. Phys. Chem. B*, , DOI:10.1021/acs.jpcb.0c05555.
51 H. Jabraoui, Y. Vaills, A. Hasnaoui, M. Badawi and S. Ouaskit, *J. Phys. Chem. B*, 2016, **120**, 13193–13205.
52 H. Jabraoui, M. Badawi, S. Lebègue and Y. Vaills, *Journal of Non-Crystalline Solids*, 2018, **499**, 142–152.
53 H. Jabraoui, E. M. Achhal, A. Hasnaoui, J.-L. Garden, Y. Vaills and S. Ouaskit, *Journal of Non-Crystalline Solids*, 2016, **448**, 16–26.
54 G. Han, X. Lu, Q. Xia, B. Lei, Y. Yan and C. J. Shang, *Journal of Alloys and Compounds*, 2018, **748**, 943–952.
55 E. A. Holm, D. L. Olmsted and S. M. Foiles, *Scripta Materialia*, 2010, **63**, 905–908.
56 G. Xiong, C. Yang, W. Zhu and H. Xiao, *RSC Advances*, 2016, **6**, 90206–90211.
57 L. Li, F. Meng, H. Tian, X. Hu, W. Zheng and C. Q. Sun, *Physical Chemistry Chemical Physics*, 2015, **17**, 9867–9872.
58 S. H. Hahn and A. C. T. van Duin, *J. Phys. Chem. C*, 2019, **123**, 15606–15617.
59 H. Jabraoui, S. Gin, T. Charpentier, R. Pollet and J.-M. Delaye, *J. Phys. Chem. C*, , DOI:10.1021/acs.jpcc.1c07266.
60 H. Jabraoui, T. Charpentier, S. Gin, J.-M. Delaye and R. Pollet, *The Journal of Chemical Physics*, 2022, **156**, 134501.
61 G. Lahiner, A. Nicollet, J. Zapata, L. Marín, N. Richard, M. D. Rouhani, C. Rossi and A. Estève, *Journal of Applied Physics*, 2017, **122**, 155105.
62 M. Mursalat, C. Huang, B. Julien, M. Schoenitz, A. Esteve, C. Rossi and E. L. Dreizin, *ACS Appl. Nano Mater.*, 2021, **4**, 3811–3820.
63 I. Abdallah, J. Zapata, G. Lahiner, B. Warot-Fonrose, J. Cure, Y. Chabal, A. Esteve and C. Rossi, *ACS Appl. Energy Mater.*, 2018, **1**, 17-62.
64 H. Wang, B. Julien, D.J. Kline, Z. Alibay, M.C. Rehwoldt, C. Rossi, and M. R. Zachariah, *J. Phys. Chem. C,* 2020*,* **124**, 25, 13679–13687